

# The Spatial Pattern of Cochlear Amplification

Jonathan A.N. Fisher,<sup>1</sup> Fumiaki Nin,<sup>1</sup> Tobias Reichenbach,<sup>1</sup> Revathy C. Uthaiyah,<sup>1</sup> and A.J. Hudspeth<sup>1,\*</sup>

<sup>1</sup>Howard Hughes Medical Institute and Laboratory of Sensory Neuroscience, The Rockefeller University, 1230 York Avenue, New York, NY 10065, USA

\*Correspondence: [hudspaj@rockefeller.edu](mailto:hudspaj@rockefeller.edu)

<http://dx.doi.org/10.1016/j.neuron.2012.09.031>

## SUMMARY

Sensorineural hearing loss, which stems primarily from the failure of mechanosensory hair cells, changes the traveling waves that transmit acoustic signals along the cochlea. However, the connection between cochlear mechanics and the amplificatory function of hair cells remains unclear. Using an optical technique that permits the targeted inactivation of prestin, a protein of outer hair cells that generates forces on the basilar membrane, we demonstrate that these forces interact locally with cochlear traveling waves to achieve enormous mechanical amplification. By perturbing amplification in narrow segments of the basilar membrane, we further show that a cochlear traveling wave accumulates gain as it approaches its peak. Analysis of these results indicates that cochlear amplification produces negative damping that counters the viscous drag impeding traveling waves; targeted photoinactivation locally interrupts this compensation. These results reveal the locus of amplification in cochlear traveling waves and connect the characteristics of normal hearing to molecular forces.

## INTRODUCTION

Human hearing is extraordinarily sensitive and discriminating. We can hear sounds down to the level of thermal fluctuations in the ear. Our ability to detect subtle differences in tones over a frequency span of three decades allows us to distinguish human voices of nearly identical timbre. We additionally perceive sounds of vastly differing intensities, enabling us to discern the strumming of nylon strings on a classical guitar playing in concert with a full orchestra. It is remarkable that the ear can achieve such sensitivity despite the viscous damping that impedes the oscillation of structures within the cochlea. Indeed, the frequency resolution of human hearing inferred from psychophysics is too great to be explained by passive resonance (Gold, 1948). Measurements of amplified, compressive vibrations within the cochlea (Rhode, 1971; Le Page and Johnstone, 1980) as well as the discovery that healthy ears produce sounds (Kemp, 1978)—so-called otoacoustic emissions—have established that the inner ear possesses an active amplification mechanism.

The qualities of active hearing can be observed in the inner ear's mechanical response to sound. A pure-tone stimulus elicits a traveling wave along the cochlear partition (von Békésy, 1960), a flexible complex of membranes that divides the spiral cochlea into three fluid-filled chambers. Increasing in amplitude as it propagates, the traveling wave peaks at a characteristic place for each specific frequency of stimulation, thereby delivering most of its energy to a select population of mechanosensory hair cells. This frequency-dependent wave profile is brought about by an interplay between longitudinal fluid coupling and local displacement of the cochlear partition, whose stiffness and mass are graded (Lighthill, 1981). In a normal ear, an active process in outer hair cells amplifies and sharpens the traveling wave, thereby fostering the remarkable frequency resolution and dynamic range that characterize healthy hearing (Rhode, 1971; Le Page and Johnstone, 1980; Sellick et al., 1982). The traveling wave of a compromised cochlea, in contrast, is diminished and broadened.

Where along the cochlear partition do active forces impart mechanical energy? A passive traveling wave conveys energy up to a resonant position that is dictated by the cochlear partition's gradient of mass and stiffness. Outer hair cells can locally inject energy that is thought to counter viscous damping and thus to augment the vibration of each segment of the partition. Because the resulting active wave can then accumulate gain by traversing the region in which amplification occurs, the cumulative gain at the wave's peak, or the integral of gain as a function of distance, is thought to dramatically exceed the local gain provided by outer hair cells (de Boer, 1983; Reichenbach and Hudspeth, 2010). Although a logical way of testing this hypothesis would be to inactivate amplification at specific positions basal to a traveling wave's peak, this has heretofore been possible only by focal ablation of hair cells (Cody, 1992). This approach reduces amplification, but at the cost of significantly altering the passive mechanical properties that transmit energy to the characteristic place.

Selectively perturbing amplification requires an understanding of the underlying active process in outer hair cells. Experiments involving isolated hair cells have identified two force-generating mechanisms. The mechanoreceptive hair bundles of many tetrapods are capable of generating forces that can be entrained by an external stimulus (Martin and Hudspeth, 1999; Kennedy et al., 2003, 2005). These forces have been observed in the form of spontaneous hair-bundle oscillations and as negative stiffness that can increase a bundle's response to low-amplitude mechanical stimulation (Martin et al., 2000, 2003). Active hair-bundle motility also contributes to nonlinear amplification in an *in vitro* preparation of the mammalian cochlea (Chan and

Hudspeth, 2005). Another force-generating mechanism specific to the outer hair cell of mammals is somatic motility or electromotility: changes in membrane potential rapidly alter the cylindrical cell's length (Brownell et al., 1985). This behavior is mediated by voltage-dependent conformational changes in the membrane protein prestin (Zheng et al., 2000), which is expressed at high levels in the basolateral plasmalemma (Huang and Santos-Sacchi, 1993). An extensive body of research on both isolated hair cells and mammalian cochleas in vivo has demonstrated the importance of functional prestin in healthy hearing (Ashmore, 2008). Mutant mice that lack prestin display substantially degraded hearing and auditory tuning curves that resemble those of a damaged cochlea (Cheatham et al., 2004). A knockin mutant mouse that expresses immotile prestin displays knockout-like hearing thresholds (Dallos et al., 2008). Because the mutant's outer hair cells appear to maintain stiffnesses similar to those in a wild-type mouse, the passive mechanical properties of the mutant's cochlea are unlikely to be significantly altered.

Although these studies demonstrate that somatic motility plays a critical role in cochlear amplification, prestin's role in shaping the cochlear traveling wave remains unclear. The interpretation of mutant studies is complicated by the fact that these modifications affect hair cells throughout the cochlea. Cochlear amplification is highly tuned; even subtle changes in the cochlea's passive properties might therefore interfere with the transmission of an acoustic signal to its characteristic place of maximal amplification. Furthermore, prestin serves as a transporter of chloride (Bai et al., 2009) and sugars (Chambard and Ashmore, 2003) and may play a significant role in maintaining physiological homeostasis in hair cells. Mutations of prestin might compromise these transporter functions.

Although a wealth of evidence suggests that hair-cell forces influence movement of the cochlear partition and vice versa, it has not been possible heretofore to locally separate the contributions of active hair-bundle motility and somatic motility. Because it affects the membrane potential, hair-bundle motility regulates somatic motility, confounding the interpretation of experiments that perturb the former mechanism. In contrast, inactivating prestin should not significantly affect hair-bundle motility. We therefore developed an optical technique that permits the targeted inactivation of somatic motility without significantly altering passive power transmission.

## RESULTS AND DISCUSSION

Active traveling waves, which are characterized by peaks that are amplified and grow nonlinearly with increasing stimulation, are notoriously difficult to visualize in vivo because surgery readily disrupts the delicate cochlea (Ren, 2002; Ren et al., 2011). By applying a scanned-beam laser interferometer in the chinchilla's cochlea, we recorded the two-dimensional profiles of the traveling waves elicited by pure tones (Figure S1A available online; Movie S1; Supplemental Experimental Procedures, Section 1). Because the chinchilla's hearing, like that of humans, is most sensitive to frequencies of a few kilohertz (Figure S1B; Heffner and Heffner, 1991), we were able to study traveling waves at frequencies relevant to human hearing.

We measured sensitive and highly compressive traveling waves on the basilar membrane, the lower surface of the cochlear partition, through a 1 mm window in the cochlea's bony wall about 2 mm apical to the round window. The basilar membrane at this position was maximally sensitive to acoustic stimulation at about 9 kHz (Figures 1A, 1B, and S1C). As the sound-pressure level (SPL) increased from about 40 dB to over 90 dB, the responses grew less steeply, a manifestation of compressive nonlinearity (Figures 1C and 1D). The peaks of active traveling waves also shifted basally as the stimulus level increased (Figures S1D and S1E). The high gain and nonlinearity were completely abolished when the active process was interrupted by anoxia (Figure 1E), which additionally displaced the wave's peak toward the cochlear base. The phase profiles of traveling waves displayed slopes that were dependent on stimulus level in healthy cochleas but not following anoxia (Figure S1F). These phenomena reflect the loss after anoxia of a tuned, tonotopically distributed amplification mechanism that enhances a traveling wave as it approaches the characteristic place at which it peaks.

To investigate the interplay between active cellular forces and the spatial shaping of an active traveling wave, we developed an optical technique that locally and significantly perturbs electromotility. Small carboxylic acids inhibit prestin-based motility; salicylate is the most effective of these blockers (Tunstall et al., 1995; Oliver et al., 2001). Our technique uses 4-azidosalicylate, the azide group of which forms covalent bonds upon activation by ultraviolet (UV) light (Figures 2A and 2B). The compound is therefore an inhibitor that forms an irreversible complex with prestin, effectively disabling it. We initially characterized the effect of 4-azidosalicylate on somatic motility in HEK293T cells transfected with prestin-eGFP. Motility was deduced from measurements of a cell's voltage-dependent capacitance, which reflects the gating currents that accompany conformational changes in large ensembles of prestin molecules. Capacitance was measured from phase changes in the currents elicited by sinusoidal membrane-potential perturbations at different holding potentials (Fidler and Fernandez, 1989). When washed onto prestin-transfected HEK293T cells, 4-azidosalicylate largely abolished somatic motility as inferred from the linearization of the voltage-capacitance relation, an effect that was reversible upon washout (Figure 2C). UV irradiation had no effect on motility in control medium (Figure 2D). If a cell incubated in 4-azidosalicylate was exposed to UV light, however, motility did not return after washout (Figures 2E and 2F). The cell nonetheless remained healthy as assessed by visual appearance and by the absence of leakage currents.

Because the nonlinear capacitance measured in prestin-expressing cells cannot be dissociated from mechanical motility (Santos-Sacchi, 1991), photoinactivation presumably elicits a concurrent attenuation of the latter. We nonetheless confirmed that photoinactivation affects the somatic motility of isolated outer hair cells. As observed in our capacitance measurements, electromotility was permanently inactivated by the combination of exposure to 4-azidosalicylate and UV irradiation, but not by either procedure alone (Figures 2G and 2I; Supplemental Experimental Procedures, Section 2). We obtained similar results from experiments on the chinchilla's cochlea in vivo

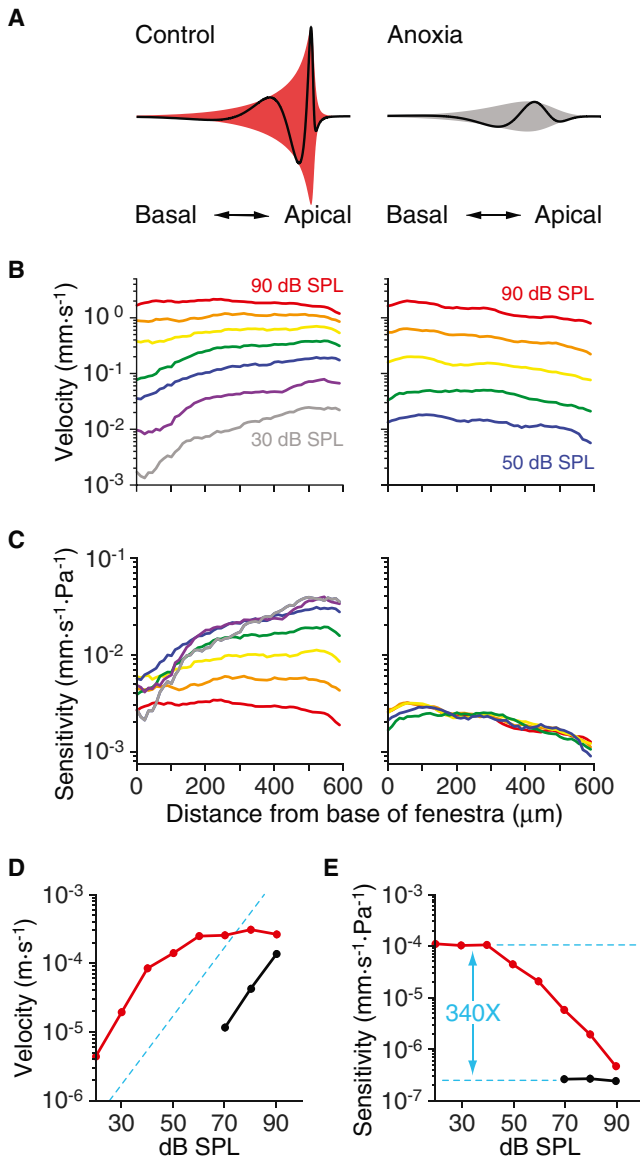


**Figure 1. Active Traveling Waves Measured In Vivo**

(A) Schematic illustrations depict the shapes of traveling waves in a normal, active cochlea (left) and an anoxic, passive one (right). The black lines show the instantaneous position of the cochlear partition; the shaded areas represent the envelopes of entire cycles of oscillation. In these diagrams and all subsequent plots of basilar-membrane data, the cochlear base lies to the left and the apex to the right.

(B) Interferometric measurements indicate the magnitudes of the velocities at which the basilar membrane oscillated up-and-down in traveling waves elicited by pure-tone stimulation at 9 kHz; the abscissa's scale is shown in (C). In this and subsequent plots of basilar-membrane data, the abscissa depicts the distance along the basilar membrane relative to the most basal point of recording. The results are plotted on a logarithmic scale and at 10 dB decrements in sound-pressure level (SPL) descending from 90 dB. As demonstrated by the convergence of the curves toward the peak, active traveling waves (left) are compressive at stimulus levels above 40 dB SPL. In contrast, the traveling waves measured in an anoxic animal (right) scale linearly with sound pressure and the peaks are shifted basally.

(C) Dividing the velocities by the stimulus pressures yields sensitivity measurements for the foregoing data. At each cochlear position, the ratio of

(Figure 3): although UV irradiation alone did not perturb the traveling wave, 4-azidosalicylate diminished the basilar membrane's movement reversibly and irradiation in the drug's presence produced a permanent deficit.

Salicylate interacts directly with prestin; the irreversible blockage of somatic motility therefore presumably reflects the covalent binding of 4-azidosalicylate to a binding site. To obtain evidence for such a direct interaction, we immunoprecipitated prestin from prestin-transfected HEK293T cells that had been incubated in 4-azidosalicylate and irradiated with UV light. Using tandem mass spectrometry, we confirmed that the final eluate contained prestin. Compared with a control sample, the prestin precipitated from photolyzed cells was predominantly oligomeric, which suggests that 4-azidosalicylate facilitates interactions between prestin protomers (Figure S2; Supplemental Experimental Procedures, Section 3). We surmise that washing 4-azidosalicylate into the scala tympani temporarily blocks motility in a large number of outer hair cells; after targeted photoinactivation and washout of the free compound, all the cells recover motility except for those that have been irradiated.

We used focal photoinactivation to probe the region at which gain occurs in active traveling waves. To guide our experiments, we computed a spatial map of cochlear-partition impedance based on measurements of active traveling waves. The local impedance  $Z(x, \omega)$  at a distance  $x$  from the cochlear base describes how a segment of the partition responds to a periodic pressure difference across it. Acoustic stimulation at an angular frequency  $\omega$  produces an oscillating pressure difference

$$p(x, t) = \tilde{p}(x, \omega)e^{i\omega t} + c.c. \quad (\text{Equation 1})$$

in which *c.c.* denotes the complex conjugate. In response, the basilar membrane oscillates at the same frequency,

$$V(x, t) = \tilde{V}(x, \omega)e^{i\omega t} + c.c. \quad (\text{Equation 2})$$

The Fourier coefficient  $\tilde{V}(x, \omega)$  follows from the pressure amplitude  $\tilde{p}(x, \omega)$  through the local impedance:

$$\tilde{V}(x, \omega) = \frac{A(x)\tilde{p}(x, \omega)}{Z(x, \omega)} \quad (\text{Equation 3})$$

in which  $A(x)$  denotes the area of a thin radial strip of the basilar membrane.

The partition's local impedance can be represented as  $Z(x, \omega) = \xi(x) + i[\omega m(x) - k(x)/\omega]$ , with a local mass  $m(x)$ , drag coefficient  $\xi(x)$ , and stiffness  $k(x)$ . The real part of the impedance therefore represents viscous damping; it is positive when viscous force impedes the partition's vibration, whereas

the maximal to the minimal sensitivity provides a measure of the wave's gain accumulated by an active cochlea (left) up to that point. Because the anoxic preparation (right) lacks gain, the sensitivity curves are superimposed.

(D) The velocities measured at the peak of the traveling wave in another control experiment (red) demonstrate compressive nonlinearity above 40 dB SPL. In contrast, the velocities in the same animal following anoxia (black) are smaller and scale linearly. The dashed line represents a linear relation.

(E) The maximal cumulative gain of the basilar membrane's active response is the ratio of the control sensitivity at low stimulus levels (red) to that following anoxia (black).

See also Figure S1.

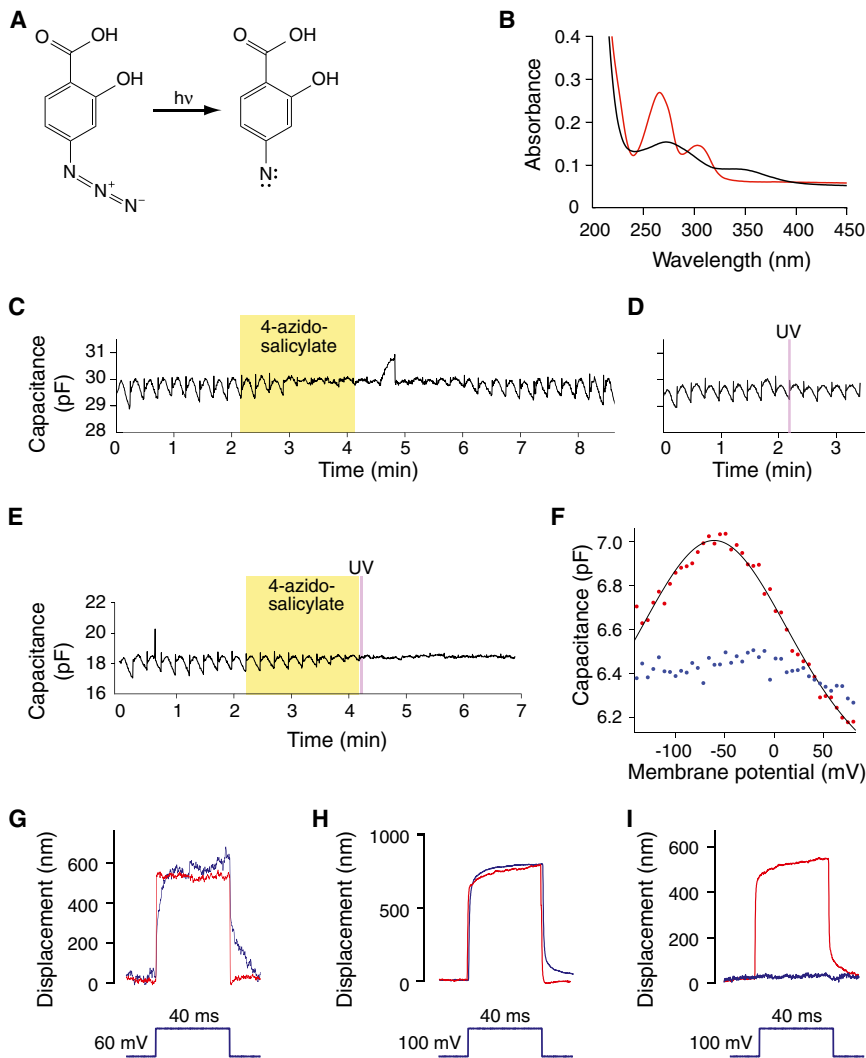


**Figure 2. Photoinactivation of Somatic Motility**

(A) UV irradiation of 4-azidosalicylate yields a highly reactive nitrene moiety that covalently attaches to nearby amino-acid residues.

(B) The optical absorbance spectrum of an aqueous solution containing 5 mM 4-azidosalicylate (red) was altered by irradiation with UV light (black).

(C) Repeated measurements from a prestin-transfected HEK293T cell showed a gradual decrease in the nonlinear capacitance during a two-minute exposure to 5 mM 4-azidosalicylate (yellow region). In the absence of exposure to UV light, the capacitance gradually returned to its baseline value as the cell was then washed with extracellular saline solution. In this and the subsequent two records, each hump represents the capacitance measured during a linear voltage ramp from a holding potential of  $-150$  to  $+100$  mV.

(D) The nonlinear capacitance in a prestin-transfected HEK293T cell was unaffected by a 1.5 s pulse of UV light.

(E) Exposure of a prestin-transfected HEK293T cell to 5 mM 4-azidosalicylate for two minutes (yellow region) abolished the nonlinear capacitance. After the cell had been irradiated with a 1 s pulse of UV light, the nonlinear capacitance did not recover following washout of the free 4-azidosalicylate.

(F) In an enlarged plot of one measurement of the voltage-dependent capacitance similar to those in (C–E), the abscissa shows the range of holding potentials over which the capacitance was measured. The nonlinear component measured in the absence of 4-azidosalicylate (red points) reflects the gating currents associated with prestin; the superimposed curve portrays a fit of the data with the derivative of a Boltzmann relation,  $C(V) = C_{LIN} + (Q_{MAX}ze/kT)e^{-ze(V-V_{1/2})/kT} [1 + e^{-ze(V-V_{1/2})/kT}]^{-2}$ , in which  $C_{LIN}$  is the linear capacitative component,  $Q_{MAX}$  is the maximal charge displacement,  $z$  is the valence,  $k$  is Boltzmann's constant,  $T$  is the absolute temperature, and  $V_{1/2}$  is the voltage at half-maximal charge

movement. The fit values are  $C_{LIN} = 5.75$  pF,  $Q_{MAX} = 0.22$  pC,  $z = 0.28$ , and  $V_{1/2} = -63$  mV. The nonlinear capacitance vanished in the presence of 5 mM 4-azidosalicylate (blue points).

(G) The changes in length of an isolated outer hair cell in response to a voltage step delivered through a wide-mouthed pipette were similar before (red) and after (blue) exposure to 5 mM 4-azidosalicylate and subsequent washout.

(H) Motility was similar for an outer hair cell isolated from a control preparation (red) and one isolated from an excised organ of Corti after exposure to UV light in the absence of drug (blue).

(I) Somatic motility was abolished in an outer hair cell isolated from an organ of Corti that was irradiated with UV light during exposure to 5 mM 4-azidosalicylate (blue). A control cell from the untreated cochlea of the same animal shows normal motility (red).

See also Figure S2.

a negative value signifies an active force that augments vibration and hence produces gain. The imaginary part of the impedance reflects stiffness, which makes a negative contribution, and inertia, whose influence has a positive sign.

We devised a mathematical technique for computing the basilar-membrane impedance, and therefore gain, based on our traveling-wave measurements. To this end, we have employed a model that depicts the cochlea as two fluid-filled chambers that are separated by a partition of graded impedance. The fluid pressure can additionally vary with both the length and the height of the cochlea's chambers (Reichenbach

and Hudspeth, 2010). The Wentzel-Kramers-Brillouin approximation yields an estimate of the velocity profile  $\vec{V}(x, \omega)$  that follows from a spatially varying impedance  $Z(x, \omega)$  (Steele and Taber, 1979; Reichenbach and Hudspeth, 2010). This approximation can conversely be used to compute the local impedance from a measured velocity profile (Figure S3; Supplemental Experimental Procedures, Section 4).

Applied to velocity measurements of active, nonlinear traveling waves, this technique revealed a region of negative damping basal to the stimulus frequency's characteristic place. In contrast, damping was everywhere positive for measurements

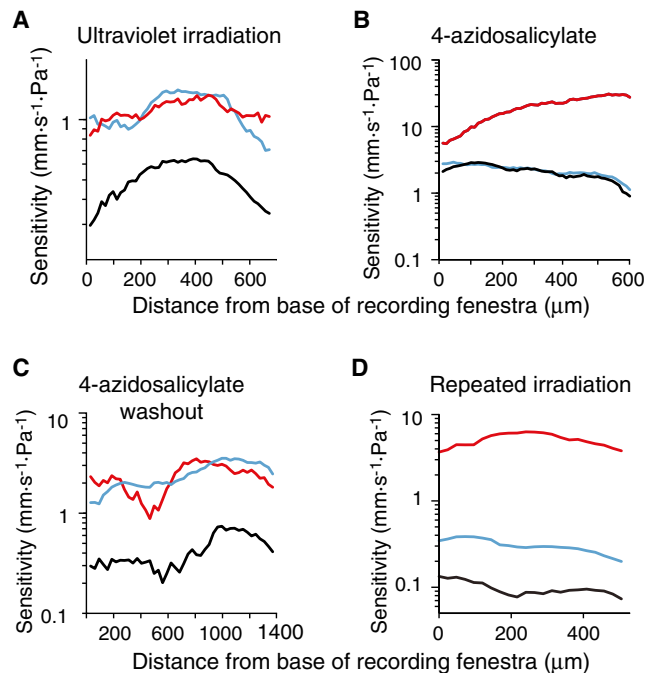


**Figure 3. The Effect of 4-Azidosalicylate and UV Light**

The most sensitive control responses, posttreatment responses, and anoxic responses measured under the specified conditions are indicated by respectively red, blue, and black lines.

(A) The sensitivity profile of an active traveling wave before and after irradiation with UV light demonstrates that the sensitivity was unaffected. The stimulus level was 60 dB SPL.

(B) While the scala tympani was perfused with 4-azidosalicylate, the traveling wave's sensitivity at 50 dB SPL fell to the level measured during anoxia.

(C) Following exposure to 7.5 mM 4-azidosalicylate and subsequent washout with artificial perilymph, the wave recovered its original sensitivity. The responses were measured at 50 dB SPL.

(D) After three bouts of irradiation over the entire exposed region of the basilar membrane during perfusion with 4-azidosalicylate, the basilar membrane's sensitivity remained roughly twice that of an anoxic preparation. The stimulus level was initially 50 dB SPL but increased to 70 dB SPL to account for the higher threshold after repeated photolysis.

See also Figure S4.

from anoxic preparations (Figures S3A and S3B). The presence of negative damping and the spatial profile of the calculated impedance support earlier theoretical predictions (de Boer, 1983). The imaginary components of the impedance were negative for all measured waves (Figure S3C), an indication that the effect of stiffness dominated that of inertia. Furthermore, the predicted values for stiffness,  $1.5\text{--}3.5\text{ N}\cdot\text{m}^{-1}$ , were similar to those measured by using compliant fibers to induce point deflections (Olson and Mountain, 1991).

Informed by the locus of amplification provided by the impedance analysis, we next sought to determine the contribution of somatic motility to local amplification. A 500  $\mu\text{m}$ -long segment of the cochlear partition that extended roughly one cycle basal from a wave's peak, depending on the location of the hole, encompassed most of the expected region of gain. Photoinactivating prestin over this broad segment reduced the sensitivity

dramatically throughout the traveling wave (Figure 4A). This result was confirmed in six additional experiments; the average sensitivity along a 50  $\mu\text{m}$  segment at the traveling wave's peak fell to  $8\% \pm 2\%$  (mean  $\pm$  SEM) of the control level. That amplification was largely eliminated by irradiation encompassing a full cycle basal to the traveling wave's peak accords with indications from studies of noise damage and compressive nonlinearity that amplification occurs primarily within a region 1–2 mm before the wave's peak (Cody, 1992). Photoinactivation significantly attenuated the local gain—the amount of gain accrued per unit length along the basilar membrane—near the wave's characteristic place (Figure S3E). Photoinactivation additionally altered the frequency tuning of the cochlear partition; after irradiation, the characteristic place for the same stimulus frequency shifted basally (Figure 4A).

Two-dimensional maps of the traveling wave in a control cochlea revealed a lag in the phase of the basilar membrane approximately beneath the outer hair cells relative to that near the spiral lamina or spiral ligament (Figure S4). The phase lag diminished during intense stimulation and vanished in the presence of 4-azidosalicylate or after anoxia. After photoinactivation, the phase pattern was radially homogeneous. Although the presence and implication of a radially varying phase profile remain controversial (Nilsen and Russell, 1999, 2000; Rhode and Recio, 2000; Homer et al., 2004), this result provides further evidence that our technique diminished the cellular forces underlying the active process.

Having established that photoinactivation of somatic motility dramatically reduces local amplification in the cochlea, we next used this tool to gauge the spatial extent of amplification and to observe how focal perturbation affects the accumulation of gain. We probed two narrow segments that extended roughly 50  $\mu\text{m}$  along the cochlear partition: one region lying a full cycle basal to the traveling wave's peak, and another situated just an eighth of a cycle before the peak. Inactivation of the more basal segment elicited a more gradual accumulation of gain; this caused a small decrement in gain that persisted, but did not increase, up to the wave's peak (Figure 4B). The modification did not significantly shift the wave's peak, suggesting that the inactivated segment lay near the beginning of the region of active amplification. This effect was confirmed in two additional experiments; the average sensitivity at the wave's peak remained  $79\% \pm 12\%$  of the control value.

Perturbation in a narrow segment near the active wave's peak, in contrast, significantly reshaped the wave, indicating that local amplification is spatially nonuniform and increases near the peak (Figure 4C). In this instance, the traveling wave initially accumulated gain at a rate similar to that under control conditions. The cumulative gain ceased to grow in the inactivated region, over which some viscous loss was evident. Finally, gain began to accumulate again just beyond the affected region. As before, the accumulation of local gain was abolished only in the segment of photoinactivation. This effect was confirmed in three additional experiments; the average sensitivity at the wave's peak was reduced to  $18\% \pm 4\%$  of the control value. After washout of 4-azidosalicylate, there were occasionally slight offset changes in the overall sensitivity, but these were not consistent (Figures 4B and 4C). However, the elimination of

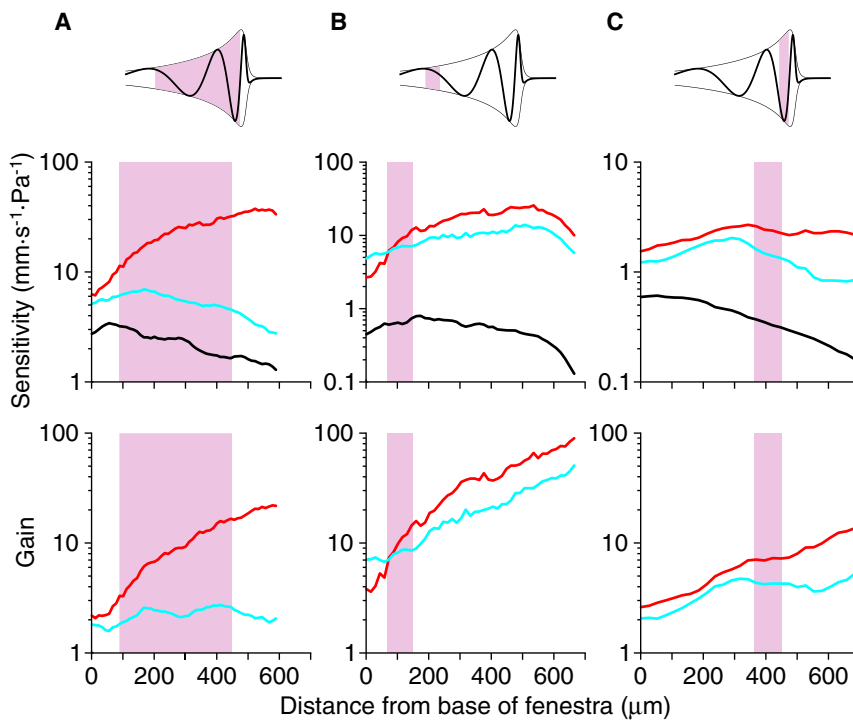


**Figure 4. Targeted Photoinactivation of Somatic Motility**

The schematic diagrams of the traveling waves atop each column, which are not drawn to scale, depict qualitatively the locus of photoinactivation. The violet-shaded area in each diagram indicates the region of UV irradiation in one of three animals. In each graph of the upper row, the red line depicts the sensitivity of a traveling wave under control circumstances and the blue line shows that after targeted photoinactivation of the specified segment of the basilar membrane. The black line indicates the sensitivity after the animal had become anoxic. In each graph of the lower row, the cumulative gain is plotted as a function of distance along the basilar membrane under control conditions (red) and after photoinactivation (blue). We define the cumulative gain at any point along the abscissa as the ratio of the point's sensitivity before to that after anoxia. (A) Photoinactivation extending roughly one cycle basal to the traveling wave's peak sharply reduced sensitivity and lowered the cumulative gain by an order of magnitude. The stimulus intensity for all lines was 50 dB SPL.

(B) Although focal inactivation well to the base of the peak locally interrupted the accumulation of gain, the sensitivity rose and gain accumulated to nearly the control level by the peak. The stimulus intensities for the red, blue, and black lines were respectively 40 dB, 40 dB, and 60 dB SPL.

(C) Focal inactivation just basal to the peak significantly diminished sensitivity; the accumulation of gain nonetheless resumed apical to the perturbation. The stimulus intensities for the red, blue, and black lines were respectively 50 dB, 50 dB, and 60 dB SPL. See also [Movie S1](#).

local gain—the slope of the cumulative gain as a function of position—occurred consistently in the photoinactivated region. In addition, focal perturbation in narrow regions locally eliminated the radial phase lag at the outer hair cells (Figure S4).

Impedance reconstructions based on these experiments indicate that inactivating the active process locally reduced negative damping and thus reveal the extent of the intrinsic positive damping by viscous forces (Figure 5). The imaginary part of the impedance did not change significantly after photoinactivation of somatic motility, suggesting that the active process has little influence on the stiffness and mass of the cochlear partition (Figure S3). This finding is consistent with observations that the intact cochlear partition is roughly three orders of magnitude stiffer than an individual outer hair cell (He and Dallos, 1999; Olson and Mountain, 1991). A portion of the active process remained after photoinactivation of regions in which gain occurred, however, for damping increased even further after anoxia (Figures 4A and 4B). Although the residual active process might reflect incomplete blockage of prestin, we ascertained that repeated exposure to UV light in the presence of 4-azidosalicylate did not further diminish the response (Figure 3D).

Understanding the degree to which photoinactivation eliminates electromotility in vivo could yield a more quantitative assessment of prestin's contribution to amplification. Obtaining a clearer picture of the intact active process would also necessitate an appreciation of the specificity with which photoinactivation affects electromotility; are other cellular processes affected? If, for example, active hair-bundle motility were entirely spared

the effects of photoinactivation, then bundle forces might account for the balance of amplification. It is possible, however, that photoinactivating prestin affected hair-bundle forces as well. Changes in an outer hair cell's membrane potential can elicit hair-bundle deflections (Jia and He, 2005). Moreover, hair bundles can be displaced by somatic length changes of outer hair cells through the mechanical coupling in an intact organ of Corti. Although adaptation in hair bundles restores the set point of nonlinear amplification even for large static deflections (Martin et al., 2003), photoinactivation might force all prestin molecules into a conformation normally elicited only by extreme depolarization. In this circumstance, active hair-bundle motility could be compromised. Finally, salicylate might affect other aspects of hair-cell physiology. Although we failed to detect photolabeling of other proteins during our biochemical investigation, it remains possible that photoinactivation modifies proteins in addition to prestin.

These results demonstrate that an active process overcomes viscous damping to locally amplify the cochlear traveling wave and that this locally accrued gain accumulates spatially up to the wave's peak. The results further indicate that prestin plays a crucial role in establishing this gain. It remains an open question, however, how this active process is locally tuned to yield a tonotopic map of amplification. Despite its critical contribution, there is no evidence yet that somatic motility exhibits resonance. Under physiological conditions, sound-evoked receptor potentials in mammalian outer hair cells modulate a resting potential of  $-40$  mV by less than 10 mV at moderate

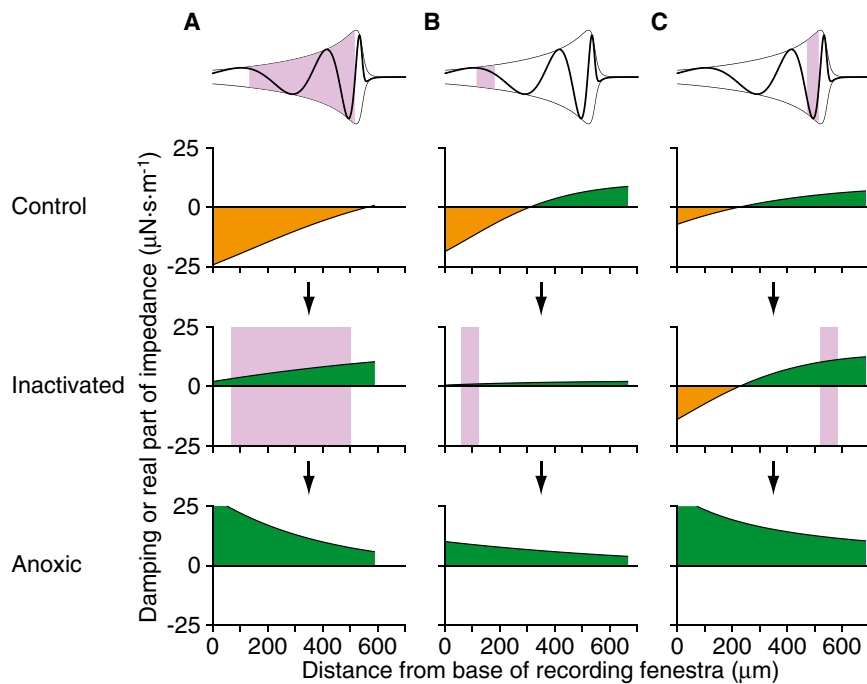


**Figure 5. Reconstructions of Local Cochlear Impedance**

For each of the three animals in Figure 4, the real part of the complex impedance, which corresponds to the dissipative force of viscous damping, is plotted for traveling waves under control conditions (top), after targeted photoinactivation (middle), and following anoxia (bottom). The regions that display net negative damping and hence active gain are shaded orange; green coloration indicates positive damping.

(A) Although irradiation of a substantial segment of the cochlear partition largely abolished negative damping, anoxia exacerbated the effect.

(B) Local inactivation of somatic motility basal to the traveling wave's peak diminished amplification. Subsequent anoxia revealed, however, that a portion of the active process persisted after photoinactivation.

(C) Inactivation of somatic motility near the peak of the traveling wave had less effect, for most of the gain had already accumulated at more basal locations.

See also Figure S3.

stimulus levels (Johnson et al., 2011; Kössl and Russell, 1992). Prestin's voltage-length relationship is almost linear in this region (Santos-Sacchi, 1991) and thus cannot alone explain nonlinear amplification. Active hair-bundle motility, in contrast, can be highly tuned (Martin and Hudspeth, 2001) and may account for the frequency selectivity and nonlinearity associated with amplification (O Maoiléidigh and Jülicher, 2010). In vivo experiments that selectively interfere with active hair-bundle motility while leaving transduction currents unperturbed might resolve this issue.

## EXPERIMENTAL PROCEDURES

### Capacitance Measurements in Prestin-Transfected Cells

Human embryonic kidney (HEK) 293T cells were cultured at 37°C in humidified air containing 5% CO<sub>2</sub> in Dulbecco's modified Eagle's medium supplemented with 10% heat-inactivated fetal bovine serum, 100 units/ml penicillin, and 100 μg/ml streptomycin (Invitrogen). The cells were transfected (Lipofectamine 2000, Invitrogen) according to the manufacturer's protocol with pEGFP-N2-prestin (Zheng et al., 2000). Fusion of GFP to either the amino or the carboxy terminus of prestin does not affect prestin's function (Ludwig et al., 2001). Cells were harvested after 24 hr of incubation.

The extracellular saline solution for electrophysiological recordings comprised 120 mM NaCl, 20 mM tetraethylammonium chloride, 2 mM MgCl<sub>2</sub>, 10 mM HEPES, and 5 mM D-glucose. The internal solution with which tight-seal pipettes were filled included 135 mM KCl, 3.5 mM MgCl<sub>2</sub>, 0.1 mM CaCl<sub>2</sub>, 5 mM K<sub>2</sub>EGTA, 2.5 mM Na<sub>2</sub>ATP, and 5 mM HEPES. Both solutions were adjusted to an osmolality of 300 mOsmol·kg<sup>-1</sup> and a pH of 7.3. In experiments that involved isolated outer hair cells, the extracellular solution was supplemented with 2 mM CoCl<sub>2</sub> to eliminate voltage-dependent ionic conductances. Solution containing 4-azidosalicylate was added to the recording chamber at a rate of 0.5–1 ml/min through a gravity-feed perfusion system controlled by a solenoid-gated pinch valve (VC-66MCS, Warner Instruments).

Whole-cell voltage-clamp recording was conducted at room temperature with borosilicate-glass microelectrodes 2–3 MΩ in resistance when filled

with internal solution. Nonlinear capacitance was measured by the phase-tracking technique, which involves analysis of the phase of the current elicited by a high-frequency sinusoidal command voltage (Fidler and Fernandez, 1989). The holding potential was sinusoidally modulated at 2.6 kHz with an amplitude of 5 mV. The series resistance and phase angle at which the current was most sensitive to capacitance changes were identified by dithering the series resistance by 500 kΩ (DR-1, Axon Instruments). The proportionality between phase change and capacitance was obtained through dithering by 100 fF the capacitance compensation of the amplifier (Axopatch 200B, Axon Instruments). Electrophysiological measurements were sampled at 12 μs intervals and analyzed with MATLAB.

### Mass Spectrometry

HEK293T cells transfected to express prestin-eGFP were incubated with 4-azidosalicylate and exposed to UV light. Prestin-eGFP was immunoprecipitated with agarose beads coated with anti-GFP and resolved by electrophoresis through a linear-gradient polyacrylamide gel. Following in-gel digestion with trypsin, the peptide extracts were analyzed by liquid chromatography-tandem mass spectrometry. Peptide identification and analysis of modified residues were conducted with the Mascot algorithm (Matrix Science).

### In Vivo Physiological Preparation

Animal procedures were performed with approval from the Institutional Animal Care and Use Committee at The Rockefeller University. In each experiment, a chinchilla (*Chinchilla lanigera*) weighing 300–500 g was anesthetized with intraperitoneally injected ketamine hydrochloride (30 mg/kg) and xylazine hydrochloride (5 mg/kg). The animal's body temperature was maintained at 37°C with a homeothermic heating pad (Stoelting). The trachea and neck musculature were exposed and a tracheotomy was performed. The pinna was then removed, the bulla opened widely through lateral and ventral approaches, and the tendons of the middle-ear muscles sectioned. A 500–700 μm hole was drilled in the basal turn of the otic capsule 1–2 mm apical to the round window, exposing a segment of the basilar membrane and permitting access for the probe beam of a laser interferometer. Through the tip of a 30G needle placed next to the hole, the scala tympani was perfused with artificial perilymph consisting of 137 mM NaCl, 5 mM KCl, 12 mM NaHCO<sub>3</sub>, 2 mM CaCl<sub>2</sub>, 1 mM MgCl<sub>2</sub>, 1 mM NaH<sub>2</sub>PO<sub>4</sub>, and 11 mM D-glucose. The solution was added at a rate of 0.5 ml/min for 1–2 min.

### Interferometric Measurements

Two-dimensional profiles of traveling waves were measured by serially scanning the beam of a heterodyne Doppler interferometer (OFV-501, Polytec) over the basilar membrane and reconstructing the spatial patterns of vibration through analysis of each scan point's complex Fourier coefficient at the stimulus frequency. No beads or other reflective elements were deposited on the basilar membrane. Heterodyne interferometric measurements of poorly reflective surfaces such as the basilar membrane are sometimes contaminated by signals from deeper surfaces of the cochlear partition (de La Roche-foucauld et al., 2005). Although the use of reflective beads can increase the signal-to-noise ratio of vibration measurements of the basilar membrane, we found that depositing beads on the basilar membrane resulted in severe spatial inhomogeneities. Because our experiments required smooth, two-dimensional measurements of a traveling wave, we avoided the use of beads. The only two other studies that have reported two-dimensional measurements of traveling waves in vivo have similarly omitted beads (Ren, 2002; Ren et al., 2011). It is nonetheless possible that these surface measurements are contaminated by internal modes of motion within the cochlear partition, an effect that could obscure the exact range and magnitude of local amplification.

Pure-tone stimuli were delivered by a calibrated sound source and the measurements were phase-locked to the stimulus waveform. Examining data in the time domain revealed no significant low-frequency modulation onto which high-frequency vibrations were superimposed. This criterion ensured that the active process was not unintentionally removed from the range of small displacements over which nonlinear amplification is significant.

### Spatially Targeted Photoinactivation of Electromotility

Interferometric measurement and photoinactivation were performed with a custom-built optical apparatus that consisted of an upright fluorescence microscope (BX51WI, Olympus) into the trinocular port of which were directed both the probe laser beam from the interferometer and the beam of a helium-cadmium laser operating at 325 nm (IK3202R-D, Kimmon Electrical).

We locally photoinactivated electromotility in vivo by scanning the beam of the 325 nm UV laser over select segments of the basilar membrane. Because the beam was loosely focused to a diameter of 10  $\mu\text{m}$ , we were able to photolyze large areas at single-cell resolution by irradiating a relatively coarse grid of scan points. A custom program (LabVIEW, National Instruments) was used to define a photolysis region and control the relevant devices. After a polygonal region was selected for photolysis on the basis of a background image of the basilar membrane, an electronic shutter (VS25S2T0-10, UniBlitz) opened long enough to permit the galvanometric mirrors to scan the UV laser beam over points on a Cartesian grid.

### SUPPLEMENTAL INFORMATION

Supplemental Information includes four figures, one movie, and Supplemental Experimental Procedures and can be found with this article online at <http://dx.doi.org/10.1016/j.neuron.2012.09.031>.

### ACKNOWLEDGMENTS

We thank B. Fabella for technical assistance; M. Vologodskaya for assistance in molecular-biological techniques; Y. Castellanos and L. Kowalik for assistance with transfection and mammalian cell culture; D. Z.-Z. He, S. Jia, and X. Tan for training on electrophysiological measurements from outer hair cells; T. Ren for discussions of traveling-wave preparations; J. Ashmore, N. Cooper, R. Fettiplace, D. Navaratnam, and M. Ruggero for comments on the experimental approach; S. Ye for discussions of azide photochemistry; N. Chandramouli for comments on photoaffinity labeling; C. Bergevin and E. Olson for discussions of sound calibration; K. Leitch for assistance with illustrations; and members of our research group for comments on the manuscript. This investigation was supported by a Bristol-Myers Squibb Postdoctoral Fellowship in Basic Neurosciences and a research grant from the American Hearing Research Foundation (to J.A.N.F.), a Career Award at the Scientific Interface from the Burroughs Wellcome Fund (to T.R.), and a Postdoctoral Fellowship

for Research Abroad from the Japan Society for the Promotion of Science (to F.N.). A.J.H. is an Investigator of Howard Hughes Medical Institute.

Accepted: September 19, 2012

Published: December 5, 2012

### REFERENCES

- Ashmore, J. (2008). Cochlear outer hair cell motility. *Physiol. Rev.* 88, 173–210.
- Bai, J.-P., Surguchev, A., Montoya, S., Aronson, P.S., Santos-Sacchi, J., and Navaratnam, D. (2009). Prestin's anion transport and voltage-sensing capabilities are independent. *Biophys. J.* 96, 3179–3186.
- Brownell, W.E., Bader, C.R., Bertrand, D., and de Ribaupierre, Y. (1985). Evoked mechanical responses of isolated cochlear outer hair cells. *Science* 227, 194–196.
- Chambard, J.-M., and Ashmore, J.F. (2003). Sugar transport by mammalian members of the SLC26 superfamily of anion-bicarbonate exchangers. *J. Physiol.* 550, 667–677.
- Chan, D.K., and Hudspeth, A.J. (2005).  $\text{Ca}^{2+}$  current-driven nonlinear amplification by the mammalian cochlea in vitro. *Nat. Neurosci.* 8, 149–155.
- Cheatham, M.A., Huynh, K.H., Gao, J., Zuo, J., and Dallos, P. (2004). Cochlear function in Prestin knockout mice. *J. Physiol.* 560, 821–830.
- Cody, A.R. (1992). Acoustic lesions in the mammalian cochlea: implications for the spatial distribution of the 'active process'. *Hear. Res.* 62, 166–172.
- Dallos, P., Wu, X., Cheatham, M.A., Gao, J., Zheng, J., Anderson, C.T., Jia, S., Wang, X., Cheng, W.H., Sengupta, S., et al. (2008). Prestin-based outer hair cell motility is necessary for mammalian cochlear amplification. *Neuron* 58, 333–339.
- de Boer, E. (1983). No sharpening? a challenge for cochlear mechanics. *J. Acoust. Soc. Am.* 73, 567–573.
- de La Rochefoucauld, O., Khanna, S.M., and Olson, E.S. (2005). Recording depth and signal competition in heterodyne interferometry. *J. Acoust. Soc. Am.* 117, 1267–1284.
- Fidler, N., and Fernandez, J.M. (1989). Phase tracking: an improved phase detection technique for cell membrane capacitance measurements. *Biophys. J.* 56, 1153–1162.
- Gold, T. (1948). Hearing II. The physical basis of the action of the cochlea. *Proc. R. Soc. Lond. B Biol. Sci.* 135, 492–498.
- He, D.Z.Z., and Dallos, P. (1999). Somatic stiffness of cochlear outer hair cells is voltage-dependent. *Proc. Natl. Acad. Sci. USA* 96, 8223–8228.
- Heffner, R.S., and Heffner, H.E. (1991). Behavioral hearing range of the chinchilla. *Hear. Res.* 52, 13–16.
- Homer, M., Champneys, A., Hunt, G., and Cooper, N. (2004). Mathematical modeling of the radial profile of basilar membrane vibrations in the inner ear. *J. Acoust. Soc. Am.* 116, 1025–1034.
- Huang, G., and Santos-Sacchi, J. (1993). Mapping the distribution of the outer hair cell motility voltage sensor by electrical amputation. *Biophys. J.* 65, 2228–2236.
- Jia, S., and He, D.Z.Z. (2005). Motility-associated hair-bundle motion in mammalian outer hair cells. *Nat. Neurosci.* 8, 1028–1034.
- Johnson, S.L., Beurg, M., Marcotti, W., and Fettiplace, R. (2011). Prestin-driven cochlear amplification is not limited by the outer hair cell membrane time constant. *Neuron* 70, 1143–1154.
- Kemp, D.T. (1978). Stimulated acoustic emissions from within the human auditory system. *J. Acoust. Soc. Am.* 64, 1386–1391.
- Kennedy, H.J., Evans, M.G., Crawford, A.C., and Fettiplace, R. (2003). Fast adaptation of mechano-electrical transducer channels in mammalian cochlear hair cells. *Nat. Neurosci.* 6, 832–836.
- Kennedy, H.J., Crawford, A.C., and Fettiplace, R. (2005). Force generation by mammalian hair bundles supports a role in cochlear amplification. *Nature* 433, 880–883.

- Kössl, M., and Russell, I.J. (1992). The phase and magnitude of hair cell receptor potentials and frequency tuning in the guinea pig cochlea. *J. Neurosci.* *12*, 1575–1586.
- Le Page, E.L., and Johnstone, B.M. (1980). Nonlinear mechanical behaviour of the basilar membrane in the basal turn of the guinea pig cochlea. *Hear. Res.* *2*, 183–189.
- Lighthill, J. (1981). Energy flow in the cochlea. *J. Fluid Mech.* *106*, 149–213.
- Ludwig, J., Oliver, D., Frank, G., Klöcker, N., Gummer, A.W., and Fakler, B. (2001). Reciprocal electromechanical properties of rat prestin: the motor molecule from rat outer hair cells. *Proc. Natl. Acad. Sci. USA* *98*, 4178–4183.
- Martin, P., and Hudspeth, A.J. (1999). Active hair-bundle movements can amplify a hair cell's response to oscillatory mechanical stimuli. *Proc. Natl. Acad. Sci. USA* *96*, 14306–14311.
- Martin, P., and Hudspeth, A.J. (2001). Compressive nonlinearity in the hair bundle's active response to mechanical stimulation. *Proc. Natl. Acad. Sci. USA* *98*, 14386–14391.
- Martin, P., Mehta, A.D., and Hudspeth, A.J. (2000). Negative hair-bundle stiffness betrays a mechanism for mechanical amplification by the hair cell. *Proc. Natl. Acad. Sci. USA* *97*, 12026–12031.
- Martin, P., Bozovic, D., Choe, Y., and Hudspeth, A.J. (2003). Spontaneous oscillation by hair bundles of the bullfrog's sacculus. *J. Neurosci.* *23*, 4533–4548.
- Nilsen, K.E., and Russell, I.J. (1999). Timing of cochlear feedback: spatial and temporal representation of a tone across the basilar membrane. *Nat. Neurosci.* *2*, 642–648.
- Nilsen, K.E., and Russell, I.J. (2000). The spatial and temporal representation of a tone on the guinea pig basilar membrane. *Proc. Natl. Acad. Sci. USA* *97*, 11751–11758.
- Oliver, D., He, D.Z., Klöcker, N., Ludwig, J., Schulte, U., Waldegger, S., Ruppersberg, J.P., Dallos, P., and Fakler, B. (2001). Intracellular anions as the voltage sensor of prestin, the outer hair cell motor protein. *Science* *292*, 2340–2343.
- Olson, E.S., and Mountain, D.C. (1991). In vivo measurement of basilar membrane stiffness. *J. Acoust. Soc. Am.* *89*, 1262–1275.
- O Maoiléidigh, D., and Jülicher, F. (2010). The interplay between active hair bundle motility and electromotility in the cochlea. *J. Acoust. Soc. Am.* *128*, 1175–1190.
- Reichenbach, T., and Hudspeth, A.J. (2010). Dual contribution to amplification in the mammalian inner ear. *Phys. Rev. Lett.* *105*, 118102.
- Ren, T. (2002). Longitudinal pattern of basilar membrane vibration in the sensitive cochlea. *Proc. Natl. Acad. Sci. USA* *99*, 17101–17106.
- Ren, T., He, W., and Gillespie, P.G. (2011). Measurement of cochlear power gain in the sensitive gerbil ear. *Nat. Commun.* *2*, 216.
- Rhode, W.S. (1971). Observations of the vibration of the basilar membrane in squirrel monkeys using the Mössbauer technique. *J. Acoust. Soc. Am.* *49*, 2, 1218.
- Rhode, W.S., and Recio, A. (2000). Study of mechanical motions in the basal region of the chinchilla cochlea. *J. Acoust. Soc. Am.* *107*, 3317–3332.
- Santos-Sacchi, J. (1991). Reversible inhibition of voltage-dependent outer hair cell motility and capacitance. *J. Neurosci.* *11*, 3096–3110.
- Sellick, P.M., Patuzzi, R., and Johnstone, B.M. (1982). Measurement of basilar membrane motion in the guinea pig using the Mössbauer technique. *J. Acoust. Soc. Am.* *72*, 131–141.
- Steele, C.R., and Taber, L.A. (1979). Comparison of WKB and finite difference calculations for a two-dimensional cochlear model. *J. Acoust. Soc. Am.* *65*, 1001–1006.
- Tunstall, M.J., Gale, J.E., and Ashmore, J.F. (1995). Action of salicylate on membrane capacitance of outer hair cells from the guinea-pig cochlea. *J. Physiol.* *485*, 739–752.
- von Békésy, G. (1960). *Experiments in Hearing* (New York: McGraw-Hill).
- Zheng, J., Shen, W., He, D.Z., Long, K.B., Madison, L.D., and Dallos, P. (2000). Prestin is the motor protein of cochlear outer hair cells. *Nature* *405*, 149–155.

# The Spatial Pattern of Cochlear Amplification

Jonathan A.N. Fisher, Fumiaki Nin, Tobias Reichenbach, Revathy C. Uthaiiah, and A.J. Hudspeth

## Supplemental Figures

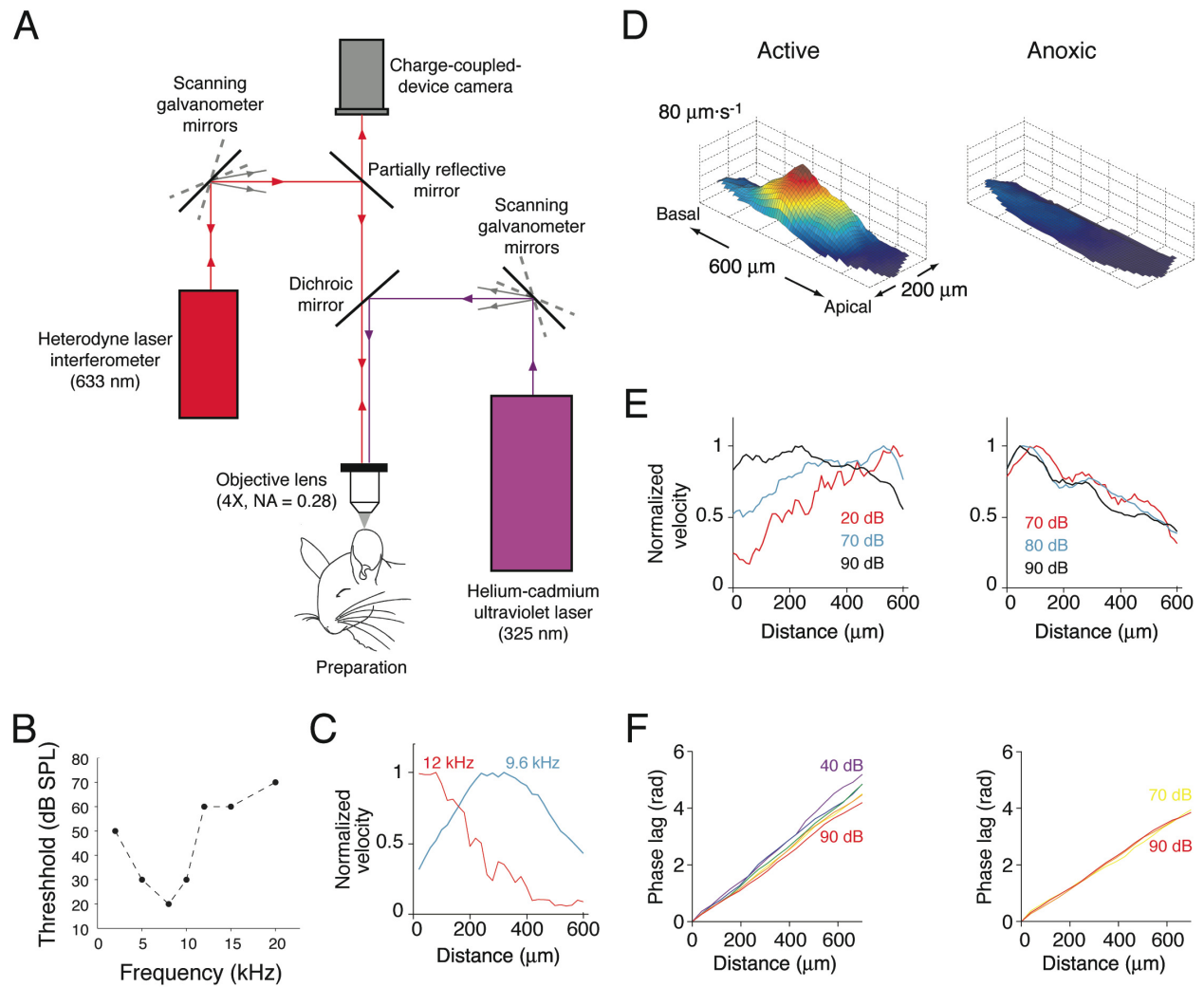


Figure S1

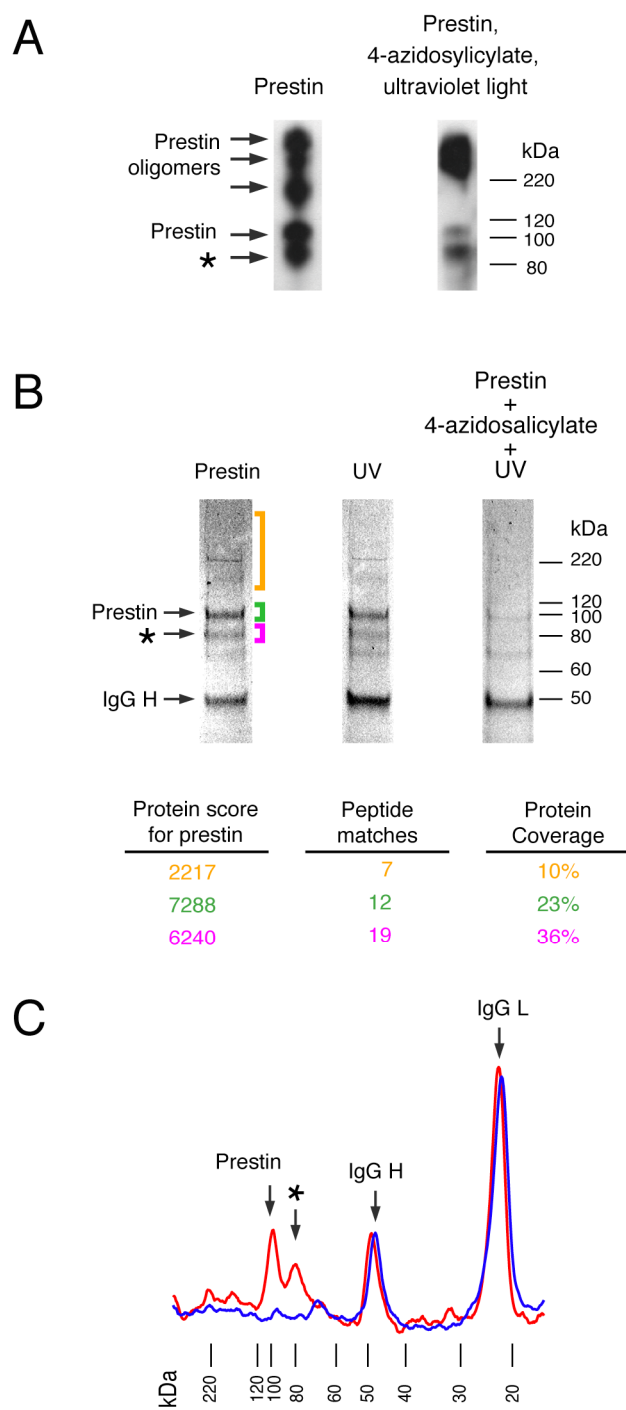


Figure S2

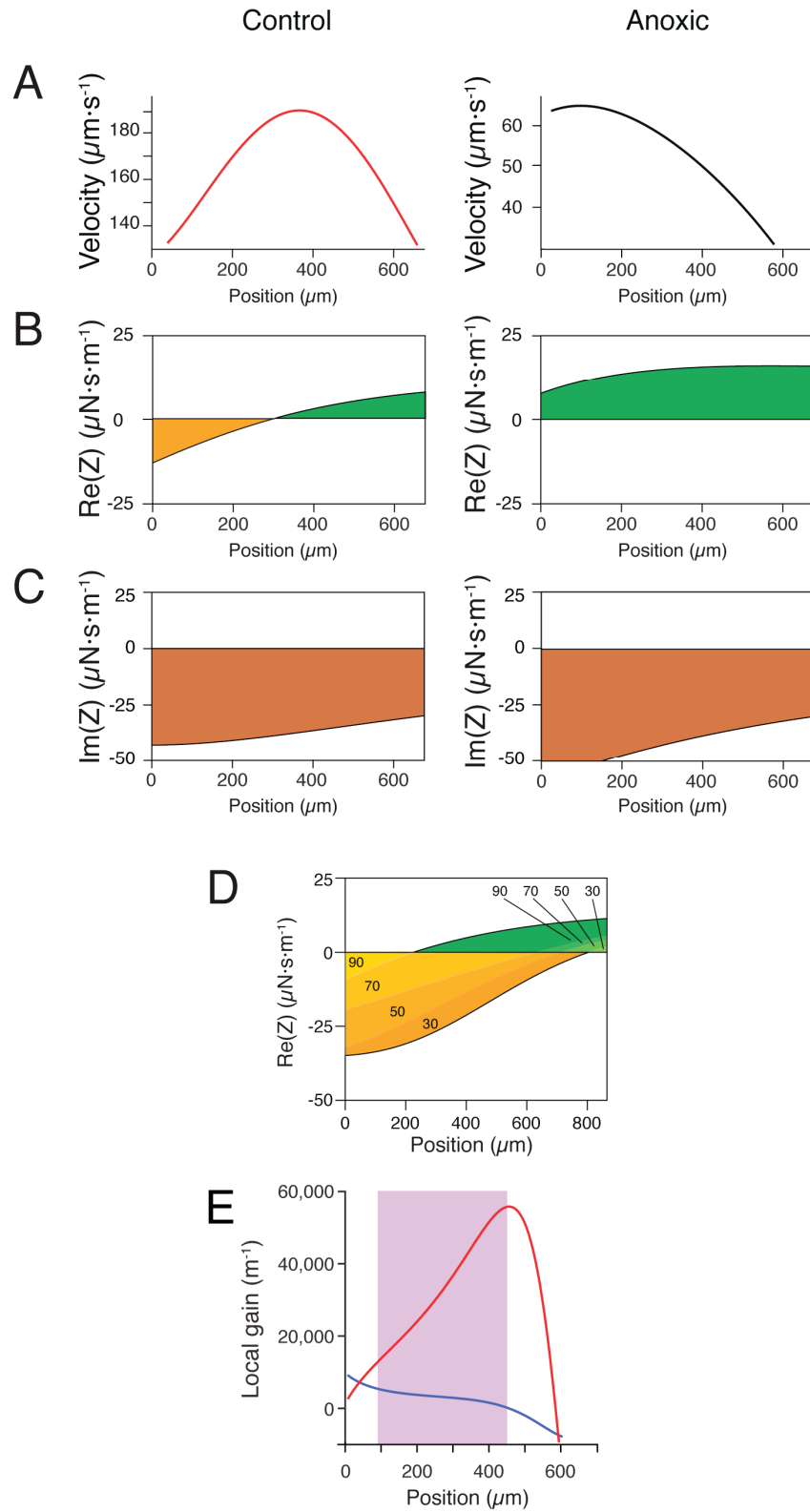


Figure S3

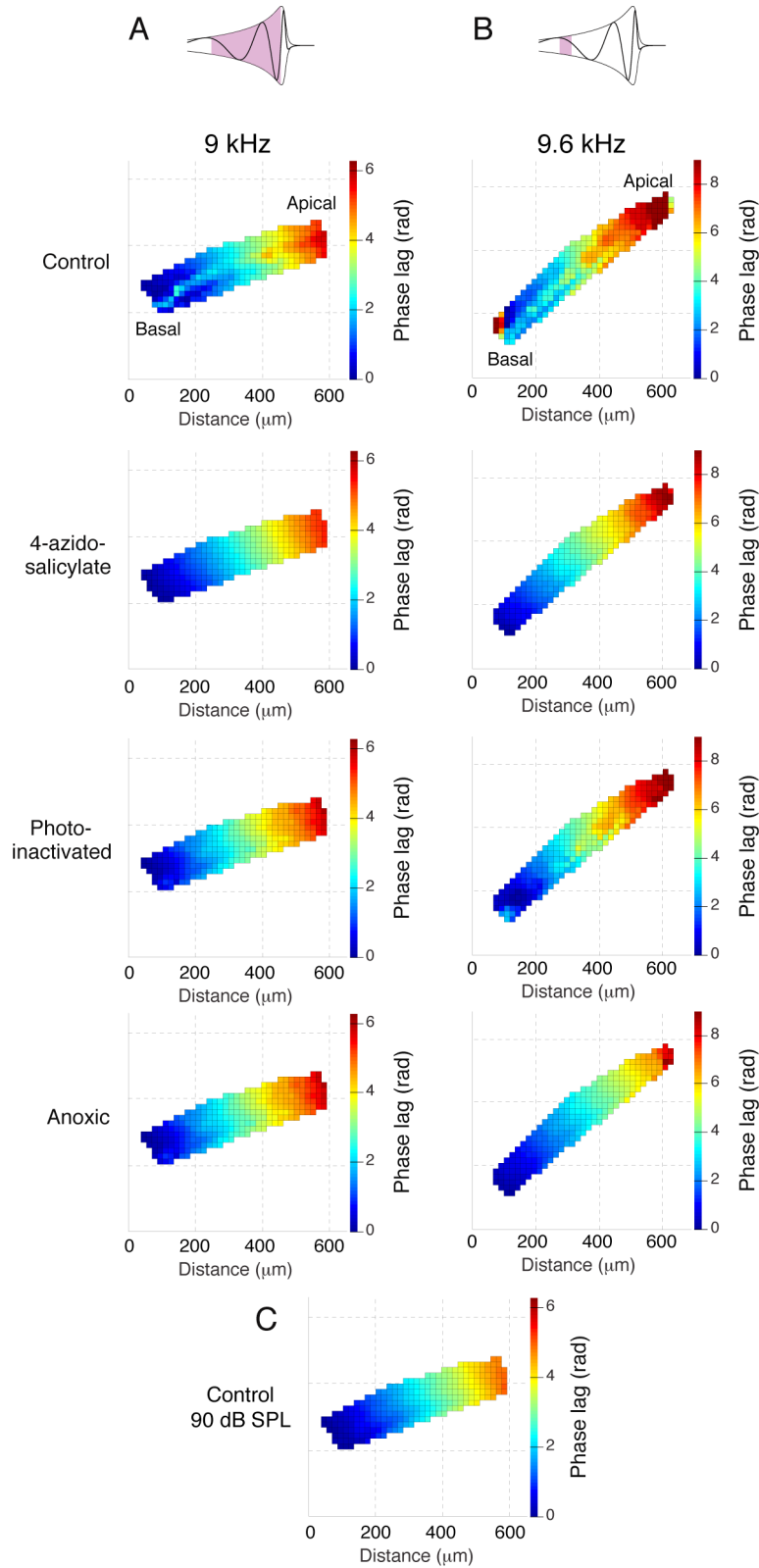


Figure S4

## Supplemental Figure Captions

**Fig. S1. Cochlear traveling waves measured *in vivo*.** (A) The probe beam of a heterodyne laser interferometer was directed into an upright microscope by galvanometric scanning mirrors that permitted velocity measurements at arbitrary positions within the microscope's field of view. The beam of a helium-cadmium ultraviolet laser was also directed into the microscope by an independent set of scanning mirrors, permitting photoinactivation of electromotility in selected regions. Contrast-enhanced images that were acquired by a charge-coupled-device camera atop the microscope provided a clear guide for selecting the regions used for interferometry and photoinactivation. The camera was also sensitive to ultraviolet light and was used to align the ultraviolet laser beam. To enhance the transmission of ultraviolet light, the microscope's tube lens was replaced with a fused silica lens of the same focal length. (B) The threshold sound-pressure level required to elicit a detectible auditory brainstem response is shown as a function of stimulus frequency for one chinchilla. Among 31 animals with sensitive hearing, the average frequency of maximal sensitivity was  $6 \pm 2$  kHz (mean  $\pm$  standard deviation). (C) To illustrate tonotopy, active traveling waves were measured in the same preparation during stimulation at 9.6 kHz and 12 kHz. (D) Plotted in three dimensions, traveling waves from active (left) and passive (right) cochleas were measured in response to a 10 kHz tone at respectively 50 dB and 60 dB SPL. The two figures are plotted on the same spatial and color scales. The vertical axes represent the absolute magnitude of the velocity. (E) Profiles of active traveling waves elicited by a 9 kHz tone (left) shifted basally with increasingly intense stimulation. In contrast, the peaks of passive waves (right) did not exhibit a shift. The velocity magnitudes for the waves have been normalized to illustrate the trends. (F) Measured in another preparation in response to a 10.8 kHz tone, the phase lags of traveling waves at different stimulus pressures revealed a dispersion (left) that vanished after anoxia (right). The sound-pressure levels varied from 90 dB (red) through 40 dB (violet) in a spectral progression. In C, E, and F, 50  $\mu$ m has been removed from both edges of the data traces because a sliding-average spatial filter required padding with zeros.

**Fig. S2. Immunoprecipitation of derivatized prestin (A)** Western blots demonstrate prestin immunoprecipitated from control cells (left) and cells that had been incubated in 4-azidosalicylate and irradiated with ultraviolet light (right). The eluate derived from agarose beads conjugated to anti-GFP contained a band corresponding to the molecular mass of monomeric prestin-eGFP (112 kDa); beneath lies a band (asterisk) that presumably corresponds to a deglycosylated form of the fusion protein. The blot additionally reveals GFP-containing bands of higher molecular mass that represent prestin oligomers. Treatment with 4-azidosalicylate and ultraviolet light yields prestin in predominantly oligomeric form. **(B)** Coomassie blue-stained polyacrylamide gels resolve immunoprecipitated prestin-eGFP. Although ultraviolet light alone had no effect, irradiation in the presence of 4-azidosalicylate caused a shift of most prestin from monomeric to oligomeric species. A band corresponding to the heavy chain of immunoglobulin G (IgG H) is also evident. We used tandem mass spectrometry to identify prestin in the gel regions that are indicated by colored brackets to the right of the prestin gel lane. Mass spectrometric analysis confirmed that all three band regions contained prestin. The protein score, matched peptides, and protein coverage are tabulated below the gel images. **(C)** The photoinactivation procedure attenuates bands observed at the molecular mass of monomeric prestin-eGFP. The bands in **B** were averaged along their width and presented as a plot of intensity in arbitrary units. The intensity profile for control (red) and treated (blue) bands are shown superimposed on the same molecular mass scale. To correct for differences in gel loading, the profiles were normalized to the band intensity of the heavy chain of immunoglobulin G, which was present to an equal extent in both samples. We further adjusted the line profiles by correcting for the inhomogeneous illumination in the gel image. A background intensity profile was traced from the gel regions just adjacent to the loaded sample lanes; this background was subtracted from the sample profiles. All profiles were smoothed with a five-point sliding average filter. Treatment with 4-azidosalicylate and ultraviolet light attenuated the bands corresponding to monomeric prestin.

**Fig. S3. Reconstruction of the cochlear partition's impedance.** The left and right panels in **A-C** represent the basilar-membrane velocities and local impedances estimated from the traveling waves in a single preparation under control conditions (left) and after anoxia (right). **(A)** The velocity profiles

from traveling waves that were measured *in vivo* were fitted with second-order polynomial functions. **(B)** In the real part of the calculated impedance, which corresponds to the degree of damping, a region of negative damping (orange) occurred basal to the position of the peak velocity in an active traveling wave. The damping associated with the anoxic wave, in contrast, was everywhere positive (green). **(C)** The imaginary part of the impedance, which reflects the cochlear partition's stiffness and mass, was negative for traveling waves under both control and anoxic conditions. These values did not change significantly between active and passive waves. **(D)** Negative damping, the signature of active amplification, diminished as the stimulus intensity grew. The magnitude of damping is indicated by color saturation; positive and negative values are indicated by respectively green and orange shading. The number in each shaded region indicates the strength of stimulation in decibels sound-pressure level. **(E)** Local gain is attenuated in the region of photoinactivation. The red line depicts the local gain of a traveling wave under control circumstances and the blue line shows that after targeted photoinactivation in the violet-shaded area. The curves show on a linear scale the spatial derivative of third-order polynomial fits to the plots of cumulative gain that are portrayed on a logarithmic scale at the bottom of Fig. 4A. Polynomial fitting was required because differentiating exacerbated the effects of noise in the recordings.

**Fig. S4. The effect of photoinactivation on the radial profiles of active traveling waves.** Panels A-C depict two-dimensional patterns of phase for the traveling waves presented in Fig. 4. Each panel shows a view of the basilar membrane from a position normal to its surface. The color bars indicate, in radians, the range of phase values. **(A)** A phase lag was observed in control measurements in the region of the outer hair cells; this lag was abolished during exposure to 4-azidosalicylate and after anoxia. **(B)** After photoinactivation of electromotility in selected regions, the phase lag was locally attenuated. **(C)** The phase pattern for a control traveling wave elicited by stimulation at 90 dB SPL revealed no radial inhomogeneity. This measurement was performed during the experiment depicted in panel A. The differences in the total longitudinal phase accumulation along the basilar membrane result primarily from the different stimulus frequencies, which are indicated at the top of the figure.

**Supplemental Movie Caption (movie available separately online)**

**Movie S1. Two-dimensional views of traveling waves.** Reconstructions from interferometric data depict cochlear traveling waves from a preparation under control conditions (top panel) and after anoxia (bottom panel). The waves travel from the base of the cochlea, which is oriented to the left, and peak at the characteristic place for the stimulus frequency. Plotting the results on identical ordinate axes emphasizes the amplification associated with active, healthy hearing. Measured in the cochlea of a single chinchilla with sensitive hearing, the waves were elicited by a 9.4 kHz tone at 70 dB SPL. The data represent interferometric measurements at points on a Cartesian grid that spanned a 175  $\mu\text{m}$   $\times$  600  $\mu\text{m}$  segment of the basilar membrane.

## Supplemental Experimental Procedures

### Section 1. Measurement of cochlear traveling waves *in vivo*

#### *Experimental apparatus*

The probe beam from a heterodyne interferometer was deflected by galvanometric scanning mirrors and directed into an upright fluorescence microscope (BX51W1, Olympus) through a beam splitter atop the microscope's auxiliary camera port (Fig. S1A). The beam from a multimode helium-cadmium laser operating at 325 nm (IK3202R-D, Kimmon Electric; 31 mW at the laser head) was routed into the same microscope port through a second, independent set of galvanometric scanning mirrors (6200, Cambridge Technology). To maximize the transmission of ultraviolet light through the optical train, the scanning and other mirrors were coated with ultraviolet-enhanced aluminum and the microscope's tube lens was replaced with a fused-silica achromatic lens of the same focal length. The final element in the optical train was a 4X, NA 0.28 low-power objective lens that offered both a large field of view and high ultraviolet transmission. The power of the ultraviolet illumination measured beneath the objective lens was 2.2 mW.

#### *Calibrated sound stimulation*

Pure-tone sound stimuli were generated by a digital signal generator (RX6), amplified with a stereo power amplifier (SA1), and delivered to an electrostatic speaker (EC1, all from Tucker Davis Technologies) whose frequency response spanned the range 4-110 kHz. The speaker was coupled by a Tygon tube to a sound-delivery assembly that was sealed into the ear canal with a 3 mm thermoplastic elastomer eartip (ER 10D-T03, Etymotic Research). The stimulus pressure was probed within the ear canal through a segment of stainless-steel hypodermic tubing 1.25 mm in inner diameter and coupled to a 0.25 in-diameter microphone (4939-A-011, Brüel & Kjær).

### *Auditory brainstem response measurement*

We assayed the hearing sensitivity of each animal by measuring the auditory brainstem response to tone pips (Fig. S1B). These sound-evoked potentials, which report activity in auditory nuclei of the brainstem, represent an objective correlate of sound perception. We defined the threshold as the least sound-pressure level at which the averaged electrical response exceeded the amplitude of the measurement noise, which was typically 5  $\mu$ V. Animals that displayed a threshold of less than 30 dB SPL at 8 kHz were considered sensitive and used in measurements of basilar-membrane motion.

The stimulus waveform consisted of a 5 ms pip of a pure tone, tapered at the onset and conclusion by 0.5 ms cosine-squared ramps. Successive tone pips were separated by 26 ms intervals, resulting in 30 pips delivered per second. Hypodermic electrodes inserted in the scalp, neck, and cheek permitted us to record referenced measurements of the evoked potentials. These signals were amplified 10,000X and band-pass filtered within a window of 300-3,000 Hz by a differential amplifier (P55, Grass Instruments) before being digitized by a multifunction data-acquisition board (PCI-6353, National Instruments). Each measurement represented the average of 1000 trials. Of the five peaks that characterize the response, the most prominent were the third and fifth, which reflect the contributions of respectively the cochlear nucleus and inferior colliculus.

### *In vivo measurements and data processing*

We measured compressive, amplified traveling waves in approximately one quarter of the preparations. The low success rate stemmed in part from the complexity and invasiveness of the surgical procedure, which often decreased an animal's hearing sensitivity. In addition, the inner-ear anatomy varied between preparations; this affected the optimal orientation of the chinchilla for interferometric recordings, which report only the component of a sample's velocity that is parallel to the probe beam. As a result, positioning the basilar membrane normal to the incident laser beam sometimes led to vignetting by the tilted plane of the hole in the cochlea. Further increases in the size of the hole to compensate for the reduction in measurement area usually resulted in non-compressive traveling waves or even standing waves. Of 21 sensitive cochleas, the traveling waves of 17 exhibited

compressive nonlinearity that persisted throughout an experiment; from these, 13 were selected for photoinactivation experiments and four for control measurements.

Traveling waves were measured by scanning either a series of points in a line along the basilar membrane or a two-dimensional array of points spanning the optically accessible segment of the basilar membrane. For both types of measurement, the distance between adjacent scan points was 18  $\mu\text{m}$ . To achieve a wide field of view, we used a low-magnification objective lens (XLFLUOR 4X/340, Olympus; 4X, NA = 0.28) that was relatively transmissive of ultraviolet light. Two-dimensional measurements were obtained by recording vibrations at points on a Cartesian grid that spanned a 180  $\mu\text{m}$ -wide strip along the basilar membrane. Single-line measurements were faster and allowed us to measure vibrations elicited by a broader range of stimulus intensities and frequencies. Because the basilar membrane's reflectivity was heterogeneous, however, single-line scans were relatively noisy. Traveling waves measured over a broad area of the basilar membrane were averaged radially to produce a smooth longitudinal profile. Although these measurements were more time-consuming, the resulting wave profiles were substantially smoother. All wave profiles were smoothed with a 10-point sliding average; the padding at the two ends of the data was subsequently removed.

We identified the characteristic frequency by varying the stimulus frequency and observing when the traveling wave's peak lay within the exposed region of the basilar membrane (Fig. S1F). Depending on the size and location of the hole in the cochlea, we were typically able to observe an accumulation of 0.75-1.5 cycles of oscillation between the hole's basal edge and the characteristic place. The wavelength additionally depended on the stimulus frequency; a higher frequency led to a lower wavelength. Active waves exhibited nonlinear compression and were amplified as much as several hundred times compared with anoxic waves (Fig. S1D; Supplemental Movie 1). With increasing stimulus intensity, an active wave's peak shifted toward the base of the cochlea (Fig. S1E). This observation was reflected in the dispersion of the traveling wave's phase (Fig. S1F): weak stimuli elicited waves that accumulated a larger phase delay over the same distance, demonstrating that active amplification is more intense for waves of smaller amplitude. The waves of anoxic animals displayed neither amplification nor intensity-dependent waveforms. These waves were broadened and displaced toward the cochlea's base.

### *In vivo photoinactivation*

To achieve the same dose of irradiation that was effective for cells in excised organs of Corti, and taking into account spectral differences in absorbance and scattering, we determined that an exposure to the laser of 15 ms per point would suffice.

### *Two-dimensional maps of phase*

Previous measurements of the basilar membrane's velocity along a line extending radially from the spiral lamina to the spiral ligament detected in active traveling waves a significant phase lead beneath the outer hair cells (Nilsen and Russell, 1999, 2000). In contrast, an anoxic wave's profile had a constant phase, describing a single mode of vibration. Although its physical basis is unclear, the phase difference suggests that an active wave involves a distinct internal mode of vibration among the various components of the cochlear partition. A radially varying phase may therefore serve as an additional hallmark of active amplification. In two-dimensional maps of phase extracted from our traveling-wave measurements, we observed a strip of phase lag along the basilar membrane at a radial position approximately beneath the outer hair cells (Fig. S4). This feature vanished from waves measured during exposure to 4-azidosalicylate, in response to high stimulus intensities, and after anoxia. The phase lag also disappeared at high intensities of stimulation, presumably because the vibrations exceeded the range of the active process. Finally, photoinactivation locally eliminated the phase lag.

## **Section 2. Photoinactivation of somatic motility**

### *Spectroscopic analysis of 4-azidosalicylate photolysis*

Dry, solid 4-azidosalicylate (US Biological) was dissolved in dimethyl sulfoxide and slowly added in 10  $\mu$ L drops to heated, stirred saline solution. The compound formed a fine precipitate that dissolved completely after 5 min of sonication in a heated water bath. The final concentration of dimethyl sulfoxide for a 7.5 mM solution of 4-azidosalicylate was 0.5% by volume. The pH was adjusted to 7.4 with NaOH.

Exposing a 5  $\mu\text{M}$  aqueous solution of 4-azidosalicylate for 10 s to 254 nm light from a hand-held lamp (EF-140C, Spectroline) caused the initially straw-colored solution to become dark yellow. Positioned 40 mm from a quartz cuvette containing the solution, the lamp provided about 200  $\mu\text{W}$  of illumination. In addition to a marked decrease in absorbance, the spectral peaks centered at 270 nm and 300 nm shifted to longer wavelengths and broadened considerably (Fig. 2B). This trend has been observed following photolysis of similar phenyl azides in aqueous solution (Budruev et al., 2004).

#### *Capacitance measurements in prestin-transfected cells*

Prestin-eGFP-transfected HEK 293T cells exhibited a bell-shaped relation of membrane capacitance to holding potentials between -150 mV and -50 mV (Fig. 2F). The nonlinear capacitance typically peaked at -90 mV, the potential at which prestin-related gating currents are most sensitive to voltage changes. The voltage-capacitance relation flattened during a 2 min exposure to 5 mM 4-azidosalicylate but recovered upon washout (Fig. 2C). Exposure to a 1.5 s pulse of 375 nm light from a diode-pumped solid-state laser (Oxxius Violet; 4.5 mW measured at the sample), equivalent to a dose of approximately  $1 \text{ MJ}\cdot\text{m}^{-2}$ , affected neither the cell's appearance nor its nonlinear voltage-capacitance relation (Fig. 2D). Power was measured with a meter capable of calibrated measurements at wavelengths as short as 325 nm (sensor S120VC and meter PM100A, Thorlabs). Although this wavelength does not coincide with an absorption peak of 4-azidosalicylate, we confirmed that the dosage was sufficient to completely photolyze the compound *in situ* by irradiating a droplet of 5 mM 4-azidosalicylate and then measuring the solution's absorbance spectrum with a micro-volume spectrophotometer (NanoDrop 2000, Thermo Scientific). We obtained a spectrum similar to that observed after light exposure of larger samples (Fig. 2B).

#### *Somatic motility measured in outer hair cells*

A Mongolian jird or gerbil (*Meriones unguiculatus*) 30-50 days of age was euthanized with intraperitoneally injected sodium pentobarbital. The auditory bulla was removed, the cochlea was exposed, and the bone of the cochlear wall was carefully chipped away with forceps to expose the stria vascularis. Unwrapping the stria vascularis from the cochlea exposed the organ of Corti. The cochlear

partition was unwound from apex to base by traction with forceps, then placed in a Petri dish containing room-temperature extracellular saline solution. This intact, excised organ of Corti was exposed to 4-azidosalicylate, ultraviolet photolysis, or a combination thereof. To simulate *in vivo* photoinactivation conditions, the organ's basilar membrane was oriented toward the ultraviolet light source.

Photoinactivation *in vivo* required that ultraviolet light penetrate the basilar membrane, auditory nerve fibers, and Deiters' cells before reaching the outer hair cells. To determine whether irradiation similar to that delivered during the experiments with HEK 293T cells sufficed for photoinactivation *in vivo*, we subjected the intact organs of Corti to the same dosage delivered from a 254 nm ultraviolet lamp (EF-140C, Spectroline). Correcting for differences in illumination intensity and absorbance at the two wavelengths, we determined that a 14-s exposure would achieve a dose of  $1 \text{ MJ}\cdot\text{m}^{-2}$ .

Following treatment, the bathing solution was removed and replaced with saline solution containing 1 mg/mL collagenase type IV. The tissue was incubated for 10 min at room temperature, then rinsed with fresh saline solution. The organ of Corti was transferred to a recording chamber where it was gently triturated with a pipette tip. Only outer hair cells 40-60  $\mu\text{m}$  in length were used. Isolated cells bathed in saline solution with  $\text{Co}^{2+}$  remained healthy for over 1 hr.

We used the microchamber technique to evoke motility (Dallos et al., 1993). The basolateral pole of an isolated outer hair cell was drawn into a wide-mouthed pipette through which current was passed; a portion of the injected current passed through the cell's interior and depolarized the cell, thereby eliciting electromotility. Glass electrodes were pulled to a diameter of 20  $\mu\text{m}$ , then fire-polished to a diameter of 10  $\mu\text{m}$ . An amplifier delivered 40 ms voltage-command pulses of 40-200 mV. We measured an outer hair cell's motility by optically monitoring the position of the cuticular plate. The cells were illuminated by a low-noise 200 W mercury-arc lamp (X-Cite Exacte, Lumen Dynamics Group Inc.) directed through the bright-field illumination port of an upright microscope (BX51WI, Olympus). The image of a cell's cuticular plate was magnified 1000X by the combination of a 40X, NA 0.80 water-immersion objective lens (LUMPlanFI/IR, Olympus) and an auxiliary telescope, then projected onto a dual photodiode connected to a circuit that calculated the normalized difference between the amounts of light falling on the two halves. Displacement was

calibrated before measurements using a piezoelectric actuator (P-840.60 and power supply E-663, Physik Instrumente) to offset the image on the photodiodes by known distances.

In response to command pulses of 100 mV, five outer hair cells exhibited length changes of  $248 \pm 48$  nm (mean  $\pm$  standard error), a value commensurate with published measurements (Hallworth, 1995). The 10 ms exponential rise in the mechanical responses, which had been observed previously, presumably reflected the electrical time constant associated with the microchamber and cell membranes. Cells that were treated with 4-azidosalicylate recovered motility after washout and were unaffected by exposure to ultraviolet light alone. In four cells that had endured exposure to both the compound and ultraviolet irradiation, however, the length changes fell to  $46 \pm 20$  nm.

Taken together, our results from measurements in HEK 293T cells and outer hair cells indicate that photoinactivation specifically impedes prestin's function and profoundly reduces the motility of hair cells.

### **Section 3. Immunoprecipitation and mass-spectrometric analysis of derivatized prestin**

#### *Immunoprecipitation of photoinactivated prestin*

Twenty-four hours after HEK 293T cells had been transfected with pEGFP-N2-prestin,  $2 \cdot 10^7$  cells were harvested into 10 mL of phosphate-buffered saline solution (PBS), washed with PBS, resuspended in PBS containing 5 mM 4-azidosalicylate, 0.5% dimethyl sulfoxide, and Pluronic F-127, and deposited in a 100 mm-diameter Petri dish. After the cells had been incubated with the compound for 3 min, the lid of the dish was removed and they were exposed for 2.5 min to 365 nm light from an ultraviolet lamp (ENB 260X, Spectroline) placed 100 mm above the plate. Following four washes with PBS, the cells were lysed at 4°C for 30 min in a solution of pH 7.4 containing 50 mM tris(hydroxymethyl)aminomethane, 150 mM NaCl, 2 mM MgCl<sub>2</sub>, 1% Igepal-40 (Sigma-Aldrich), 0.5% deoxycholate, 0.1% sodium dodecyl sulfate, and Complete Protease Inhibitor (Roche). After centrifugation at 13,200 X g and at 4°C for 60 min, the soluble fraction was mixed with agarose beads coated with anti-GFP (Fusion Aid GFP Kit, Vector Labs) and incubated with rocking at 4°C for 2 hr. The agarose beads were then collected and washed three times with a solution identical to the

foregoing but lacking deoxycholate. The precipitated protein complex was eluted from the beads by boiling for 5 min in NuPAGE LDS sample-loading buffer solution (Invitrogen). Proteins were resolved on a 4-12% gradient 2-[bis(2-hydroxyethyl)amino]-2-(hydroxymethyl)-1,3-propanediol polyacrylamide gel (NuPAGE, Invitrogen). Gel bands were revealed by staining with Coomassie blue (GelCode Blue Stain, Pierce). To identify bands that contained GFP on Western blots, we transferred proteins to nitrocellulose membranes with a semi-dry electrophoretic transfer cell (Trans-Blot SD, Biorad) and immunoblotted with an anti-GFP antibody (Millipore). Labeled bands were visualized with a chemiluminescence kit (RPN2132, Amersham) and Bio-Mark MS film (Sigma-Aldrich).

Immunoprecipitation of prestin-eGFP from HEK 293T cells yielded a nearly background-free eluate that displayed a prominent band at 112 kDa, the mass of a prestin-eGFP monomer (Fig. S2A,B). A 90 kDa band also occurred; this probably represented a deglycosylated form of the fusion protein (Matsuda et al., 2004). In a Western blot that was probed with an anti-GFP antibody, GFP was additionally identified at higher multiples of prestin's monomeric weight. The latter bands correspond to a range of prestin multimers that have been described previously (Zheng et al., 2006; Detro-Dassen et al., 2008). Photoinactivation increases the relative fraction of these multimeric forms; this trend is visible in a quantitative analysis of the gel bands (Fig. S2C). Compared with a control sample, bands at the molecular mass of monomeric prestin-eGFP are absent in the irradiated sample. The absence of an increased intensity in the regions of higher molecular mass in the treated sample is possibly due to the diffuse distribution of prestin's multimeric forms within the gel.

#### *Liquid chromatography-tandem mass spectrometry (LC-MS/MS)*

Gel bands corresponding to monomeric prestin were excised from gels and subjected to in-gel trypsin digestion and peptide extraction (Kumarathasan et al., 2005). After reduction with 10 mM dithiothreitol, alkylation with 55 mM iodoacetamide, and digestion overnight at 37°C with sequencing-grade modified trypsin (Promega) in ammonium bicarbonate buffer solution, the products were extracted twice with 0.1% trifluoroacetic acid and 50% acetonitrile. The extracted mixture was dried and dissolved in 10 mL 0.1% trifluoroacetic acid.

The extracts were subjected to LC-MS/MS analysis. The pool of peptides was first separated on a reverse-phase column in a high-performance liquid-chromatography system (U3000, Dionex) at a flow rate of 250 mL/min, then directly introduced by electrospray into an LTQ-Orbitrap mass spectrometer (Thermo Fisher) operating in data-dependent-scan mode. A fused-silica capillary column 75 mm in internal diameter and 100 mm in length (Upchurch Scientific) was packed with C-18 resin (300 Å, Varian). Mobile phase solvent A contained 0.1% formic acid and mobile phase solvent B contained 99.9% acetonitrile and 0.1% formic acid. One-hour gradient runs were performed in solvent B with a flow rate of 250 nL/min. The mass-acquisition method involved one mass-spectrometric scan followed by six tandem scans in the ion trap. The initial scan acquired ionic species with mass-to-charge ratios of 400-1600. The six most intense peaks from each scan were selected in the ion trap for further fragmentation and tandem mass spectrometry.

The resultant peptides, as well as their parent proteins, were identified in the NCBI non-redundant database NCBI nr for Chordata with the Mascot algorithm (Matrix Science Inc.) and the following parameter settings: missed cleavage, 1; fixed modification, carbamidomethylation; variable modification, photo-labeling; and oxidation, m. The maximum error tolerance was 20 ppm for mass-spectrometric scans and 1.2 Da for tandem scans. We used stringent criteria for protein identification, selecting only those peptides with an ion score of at least 40. The protein score is described by  $-10 \cdot \log(p)$ , in which  $p$  is the probability that the observed match is a random event. Protein scores greater than 70 are significant based on the Mascot scoring algorithm that uses a threshold of  $p < 0.05$ . Individual ion scores for peptides exceeding 38 indicate identity or extensive homology at the level  $p < 0.05$ .

We identified roughly 10-35% of the trypsin-digested peptide sequences in all experiments. Mass spectrometry demonstrated prestin in all of the three analyzed bands: the oligomeric, 112 kDa, and 90 kDa gel bands.

#### **Section 4. Estimation of basilar-membrane impedance**

Acoustic stimulation at an angular frequency  $\omega$  produces an oscillating basilar-membrane velocity

$$V(x, t) = \tilde{V}(x)e^{i\omega t} + c.c. \quad (1)$$

in which  $x$  is the coordinate along the membrane's midline and  $c.c.$  denotes the complex conjugate. Here and in the following equations we omit the dependence on  $\omega$ . Laser interferometry measures the Fourier component  $\tilde{V}(x)$  and shows that the velocity propagates as a wave with a local vector  $k(x)$ :

$$\tilde{V}(x) = a(x) \exp\left[-i \int_0^x dx' k(x')\right]. \quad (2)$$

The local wave vector depends on the membrane's local impedance  $Z(x)$ . Because the impedance changes from the base of the cochlear to its apex, the wave vector is also spatially dependent. The Wentzel-Kramers-Brillouin approximation provides an analytical expression to relate the impedance to the wave vector:

$$-2i\rho\omega A = Z(x)k(x)\tanh[k(x)h], \quad (4)$$

in which  $h$  denotes the height of the scalae and  $\rho$  the density of their liquid contents (Steele and Taber, 1979; Lighthill, 1981; Reichenbach and Hudspeth, 2010).

Two limiting cases are instructive. First, if the wavelength is smaller than the height of the scalae,  $|k(x)h| \gg 1$ , we can approximate  $\tanh[k(x)h] \approx \text{sgn}[k(x)]$  and obtain

$$-2i\rho\omega A = Z(x)|k(x)|. \quad (5)$$

In the second instance, when the wavelength exceeds the height of the scalae,  $|k(x)h| \ll 1$ ,  $\tanh[k(x)h] \approx k(x)h$  and thus

$$-2i\rho\omega A = Z(x)k^2(x)h. \quad (6)$$

The Wentzel-Kramers-Brillouin approximation also yields an estimate of the velocity's amplitude variation:

$$a(x) = k^\beta(x), \quad (7)$$

in which  $\beta = 1/2$  applies in the short-wavelength case and  $\beta = 3/2$  in the long-wavelength situation.

In the inverse problem posed by the present experiments, how can the basilar-membrane impedance  $Z(x)$  be computed from measurements of the velocity  $\tilde{V}(x)$ ? Denote as  $g(x) = \int_0^x dx' k(x')$  the phase of the Fourier component  $\tilde{V}(x)$ . The wave vector follows as the derivative,  $k(x) = dg(x)/dx$ . Equations 2 and 7 yield an equation for the phase:

$$g(x) = i \ln[\tilde{V}(x)] - i\beta \ln[k(x)]. \quad (8)$$

This equation cannot be solved for  $g(x)$  directly; we must therefore employ successive approximations. To a first approximation, in which the amplitude  $a(x)$  is assumed to be constant, an estimate of  $g(x)$  follows as

$$g_1(x) = i \ln[\tilde{V}(x)]. \quad (9)$$

From  $g_1(x)$  we obtain the initial estimate of the wave vector,  $k_1(x) = dg_1(x)/dx$ . We then use  $k_1(x)$  to compute a second approximation for the phase,

$$g_2(x) = i \ln[\tilde{V}(x)] - i\beta \ln[k_1(x)], \quad (10)$$

which leads to a second approximation for the wave vector,  $k_2(x) = dg_2(x)/dx$ . We iterate this procedure  $n$  times, in which

$$g_n(x) = i \ln[\tilde{V}(x)] - i\beta \ln[k_{n-1}(x)] \quad (11)$$

and

$$k_n(x) = \frac{dg_n(x)}{dx}. \quad (12)$$

These approximations converge after a few iterations to yield the functions  $g(x)$  and  $k(x)$ .

In our computations we initially approximated the magnitude and phase of the velocity  $\tilde{V}(x)$  through a second-order polynomial fit (Fig. S3A). We then determined the functions  $g(x)$  and  $k(x)$  through the successive approximations outlined above. The impedance  $Z(x)$  followed from Equation 5 or 6, in which we assumed a liquid density  $\rho = 10^3 \text{ kg}\cdot\text{m}^{-3}$ , a scala height  $h = 1 \text{ mm}$ , and a rectangular area  $A$  of  $8 \text{ }\mu\text{m}$  breadth and  $300 \text{ }\mu\text{m}$  width.

Using this reconstruction technique, we calculated the basilar-membrane impedance for active and anoxic traveling waves (Fig. S3B,C). We used the large-chamber-height approximation (Eq. 5) because the wavelength was substantially smaller than the chamber height at the location in the chinchilla's basal turn where we performed our measurements.

The real part of the reconstructed impedance, which represents viscous damping, was negative in the region leading up to the peak of an active traveling wave (Fig. S3B). This negative damping disappeared after anoxia and declined with increasing stimulus intensity (Fig. S3D), demonstrating that

negative damping is correlated with a wave's gain. In contrast, for both active and passive waves, the imaginary part of the calculated impedance was entirely negative (Fig. S3C). This result indicates that the effect of stiffness dominated that of mass in the region of interest. Furthermore, the value of the imaginary part did not change significantly after anoxia; this effect suggests that stiffness was independent of cochlear amplification.

### Supplemental References

- Budruev, A. V., Karyakina, L. N., and Oleinik, A. V. (2004). Photolysis of ortho-azidobenzoic acid in aqueous solutions and water-organic solvent mixtures. *High Energ. Chem.* 38, 20-24.
- Dallos, P., Hallworth, R., and Evans, B. N. (1993). Theory of electrically driven shape changes of cochlear outer hair cells. *J. Neurophysiol.* 70, 299-323.
- Detro-Dassen, S. et al. (2008). Conserved dimeric subunit stoichiometry of SLC26 multifunctional anion exchangers. *J. Biol. Chem.* 283, 4177-4188.
- Hallworth, R. (1995). The biomechanics of outer hair cell motility. in *Active Hearing*. Flock, O., and Ulfendahl, M., eds. (Oxford: Pergamon), pp. 155-166.
- Kumarathasan, P., Mohottalage, S., Goegan, P., and Vincent, R. (2005). An optimized protein in-gel digest method for reliable proteome characterization by MALDI-TOF-MS analysis. *Anal. Biochem.* 346, 85-89.
- Matsuda, K. et al. (2004). N-linked glycosylation sites of the motor protein prestin: effects on membrane targeting and electrophysiological function. *J. Neurochem.* 89, 928-938.
- Zheng, J. et al. (2005). The C-terminus of prestin influences nonlinear capacitance and plasma membrane targeting. *J. Cell Sci.* 118, 2987-2996.
- Zheng, J. et al. (2006). Analysis of the oligomeric structure of the motor protein prestin. *J. Biol. Chem.* 281, 19916-19924.